PROCEEDINGS A

rspa.royalsocietypublishing.org

Research

Article submitted to journal

Subject Areas:
mechanical engineering

Keywords:
Nonlinear normal mode (NNM); Bifurcations; Internal resonance; Mathieu equation.

Author for correspondence:
Dongxiao Hong
e-mail: dx.hong@bristol.ac.uk

THE ROYAL SOCIETY
PUBLISHING

Existence and location of internal resonance of two-mode nonlinear conservative oscillators

Dongxiao Hong, Thomas L. Hill and Simon A. Neild

Department of Mechanical Engineering, University of Bristol, Bristol BS8 1TR, UK

Internal resonances can be widely observed in nonlinear systems; even a simple nonlinear system can exhibit intricate internal resonances when vibrating at large amplitudes. In this study, the existence and locations of internal resonances of a general two-mode system with an arbitrary eigenfrequency ratio are considered. This is achieved by first considering the symmetric case, where the internal resonances are found to be approximately captured by the Mathieu equation. It is shown that the bifurcations can exist in pairs; and, for each pair, the bifurcated solution branches capture modal interactions with the same commensurate frequency relationship but different phase relationships. To determine the existence and locations of internal resonances the divergence and convergence for correlated bifurcation pairs are then considered. Lastly, the internal resonances in asymmetric cases are analytically derived, where the asymmetry induced bifurcation splitting is captured by a non-homogeneous extended Mathieu equation. This work explores the mechanism underpinning internal resonances, and explains their topological features, such as which internal resonances are observed as amplitude increases. A graphical method is also proposed for efficient determination of the existence and locations of internal resonances.

1. Introduction

Nonlinear systems can exhibit intricate dynamic behaviours that cannot be seen in linear counterparts, e.g. internal resonances, bifurcations, instability and chaos [1,2]. Among these, internal resonances are captured by modal interactions and are governed by

equations of motion in which nonlinear terms couple the different modal components. Such nonlinear phenomena have been extensively observed and studied in many mechanical systems, e.g. cables [3,4], beams [5–8], and shells [9]; as such, quantifying internal resonances is important in modelling these systems. On the other hand, exploiting the energy transfer triggered by internal resonances has given rise to promising engineering applications such as vibration suppression [10–12], and energy harvesting [13,14].

The presence of internal resonance can be linked to the commensurate relationships between the *nonlinear response frequencies* of the interacting modes. This results in the established terminology of a $m:n$ internal, or autoparametric, resonance [15,16], where m and n denote the commensurate frequency matches of modes. For nonlinear systems vibrating at small to moderate amplitudes, the detuning between the eigenfrequency and nonlinear frequency is small; in this case, the types of internal resonances can be approximately determined by referring to the ratio of eigenfrequencies [17]. For example, two coupling modes with an eigenfrequency ratio of approximately $1:3$ is expected to exhibit a $1:3$ internal resonance. Extensive works, addressing particular types of internal resonances, can be found in a wide range of systems [3–9,18–20]. In practice, fully exploiting the performance of nonlinear systems may lead to large-amplitude responses. In this region, the small detuning condition is no longer satisfied and the analysis of internal resonances becomes challenging due to the necessity of access to the nonlinear frequency [17]. In this case, a series of intricate internal resonances can exist, even in a simple two-mode system [21–23]; however, the existence of internal resonances is usually determined via numerical simulations and case-by-case studies. The existence and locations of internal resonances for an arbitrary system, regardless of the response frequency range, remains an open problem.

Besides the commensurability of nonlinear frequencies, an alternative tool to characterise an internal resonance is referring to the geometric feature of responses via the concept of nonlinear normal modes (NNMs). This approach was introduced by Rosenberg [24,25], where an NNM is defined as a family of synchronous periodic responses of a conservative system. It requires that the motions of *all* components reach their extrema and equilibrium points simultaneously. This definition was later extended to periodic responses (not necessarily synchronous) of a conservative system in [21]. For dissipative systems, alternative definitions include an invariant manifold tangent to a linear modal subspace at the origin [26], and the smoothest invariant manifold of a spectral subspace, i.e. a spectral submanifold (SSM) [27]. In [4,28,29], synchronous and asynchronous NNMs were studied for nonlinear systems with $1:1$ internal resonances. However, more general scenarios of $m:n$ internal resonances, and how these two geometrically different synchronous and asynchronous responses are connected, to the best knowledge of the authors, have not yet been addressed.

In this paper, we study the existence and locations of internal resonances for conservative nonlinear systems using the concept of NNMs [21]. In §2, the motivating example of a two-mode beam is first considered. When vibrating at large amplitudes, we show the existence of intricate internal resonances, where multiple commensurate relationships of nonlinear frequencies are satisfied. To account for the geometry of internal resonances in the configuration space, the NNMs are re-generalised by referring to the Fourier components of the interacting modes. In accordance with this generalisation, we propose the terminology of *Fourier-real* and *Fourier-complex* NNMs. In §3, in order to explain and interpret the topological features of internal resonances, the specific example is extended to a general two-mode system with an arbitrary eigenfrequency ratio. The mixed-mode NNMs, in the neighbourhood of the primary single-mode NNM branch, is derived, and shown to be approximately captured by the Mathieu equation, whose solution sets are associated with the Fourier-real and Fourier-complex generalisations. In addition, on the primary NNM branch, the bifurcations that lead to mixed-mode NNMs are shown to exist in pairs. For each pair, the bifurcated solutions show interacting modes with the same frequency commensurability but with different Fourier components, or phase relationships. Considering the converging and diverging behaviours of such pairs, the existence and locations of internal resonances can be determined. In §4, the symmetry breaking induced bifurcation splitting of

internal resonances is derived and shown to be captured by an extended nonhomogeneous Mathieu equation. Finally, conclusions are presented in §5.

2. Internal resonances in two-mode systems

In this section, a two-mode conservative system, with cubic nonlinearities, is considered. Such a two-mode system is representative of many mechanical systems with two interacting modes, e.g. a pinned-pinned beam [23], a vibration absorber attached to a primary system [19], or a rotor system [28]. The governing equations of motion are given by

$$\ddot{q}_r + \omega_{nr}^2 q_r + \Psi_{4,0} q_r^3 + 3\Psi_{3,1} q_r^2 q_s + \Psi_{2,2} q_r q_s^2 + \Psi_{1,3} q_s^3 = 0\,, \tag{2.1a}$$

$$\ddot{q}_s + \omega_{ns}^2 q_s + \Psi_{3,1} q_r^3 + \Psi_{2,2} q_r^2 q_s + 3\Psi_{1,3} q_r q_s^2 + \Psi_{0,4} q_s^3 = 0\,, \tag{2.1b}$$

where q_r and q_s denote linear modal displacements of two interacting modes, whose eigenfrequencies are ω_{nr} and ω_{ns} respectively, and $\Psi_{m,n}$ are nonlinear coefficients, where m and n denote the exponent of q_r and q_s respectively for the Lagrangian, written as

$$\mathcal{L} = \frac{1}{2}\dot{q}_r^2 + \frac{1}{2}\dot{q}_s^2 - \frac{1}{2}\omega_{nr}^2 q_r^2 - \frac{1}{2}\omega_{ns}^2 q_s^2 - \frac{1}{4}\Psi_{4,0} q_r^4 - \Psi_{3,1} q_r^3 q_s - \frac{1}{2}\Psi_{2,2} q_r^2 q_s^2 - \Psi_{1,3} q_r q_s^3 - \frac{1}{4}\Psi_{0,4} q_s^4\,. \tag{2.2}$$

Such a two-mode model (2.1) can also be derived via the Galerkin's method using a two-mode truncation. Here, we consider a pinned-pinned beam with a two-mode truncation and show the intricate modal interactions between the first two modes, q_r and q_s, when vibrating at large amplitudes. The parameters of the equations, i.e. $\omega_{nr}, \omega_{ns}, \Psi_{4,0}, \ldots, \Psi_{0,4}$ can be obtained during the Galerkin's procedure, applied to a von Kármán model, i.e.

$$\rho A \frac{\partial^2 w(x,t)}{\partial t^2} + EI \frac{\partial^4 w(x,t)}{\partial x^4} - N \frac{\partial^2 w(x,t)}{\partial x^2} = 0\,, \tag{2.3}$$

where ρ, A, E, I and N denote the density, cross-sectional area, Young's modulus, second moment of area and axial force of the beam, respectively, and where $w(x,t)$ represents the transverse displacement at axial position x at time t. As this motivating example is used for illustration rather than providing a complete study on beam dynamics, the derivations of the coefficients are not provided here; however, interested readers are directed to references [5,23,30] for details.

Here, an example system with $\omega_{nr} = \pi^2$, $\omega_{ns} = 4\pi^2$, $\Psi_{3,1} = \Psi_{1,3} = 0$, $\Psi_{2,2} = 2\pi^4$, $\Psi_{4,0} = \pi^4/2$ and $\Psi_{0,4} = 8\pi^4$ is considered; this represents a dimensionless two-mode truncation of a pinned-pinned beam, derived in [5,23]. Note that, due to the symmetric configuration, such a beam system has $\Psi_{3,1} = \Psi_{1,3} = 0$. The NNM branches, or backbone curves, are computed via numerical continuation package COCO [31], and shown as the frequency-amplitude plot and frequency-energy plot in panels (a) and (b) respectively in figure 1 to aid comparison[1]. The primary NNM branch, S_r, emerges from the eigenfrequency, ω_{nr}, and contains only q_r components. Four further NNM branches, emerging from modal interactions between q_r and q_s, bifurcate from the primary branch via pitchfork bifurcations [23]. By considering the schematic time-parameterised responses of these four mixed-mode solution branches, shown in panels $(c), (d), (e)$ and (f), it can be seen that the modal frequencies are commensurate. The correlated internal resonances can be categorised by accounting for this frequency commensurate relationship between the two interacting modes, resulting in the internal resonances being classified as $1:3$ internal resonances (see panels (c) and (d)), and $1:2$ internal resonances (i.e. panels (e) and (f)). An alternative method to check the $1:3$ commensurability is dividing the response frequency of S_s by three, where the two mixed-mode NNM branches intersect S_s, see panels (a) and (b). Analysis of internal resonances of the beam system can also be found in [5,23].

The internal resonances can also be specified by referring to Rosenberg's definition of NNMs, where panel (d) represents a synchronous NNM [24,25]; whilst the other panels, (c), (e) and (f), are asynchronous [21]. Having geometrically different NNM solutions defined using the same terminology is certainly less than optimal. To obtain a *unique* classification for each NNM, and

[1]Note that, in the following study, we chose the frequency-amplitude projection for interpretations and analysis.

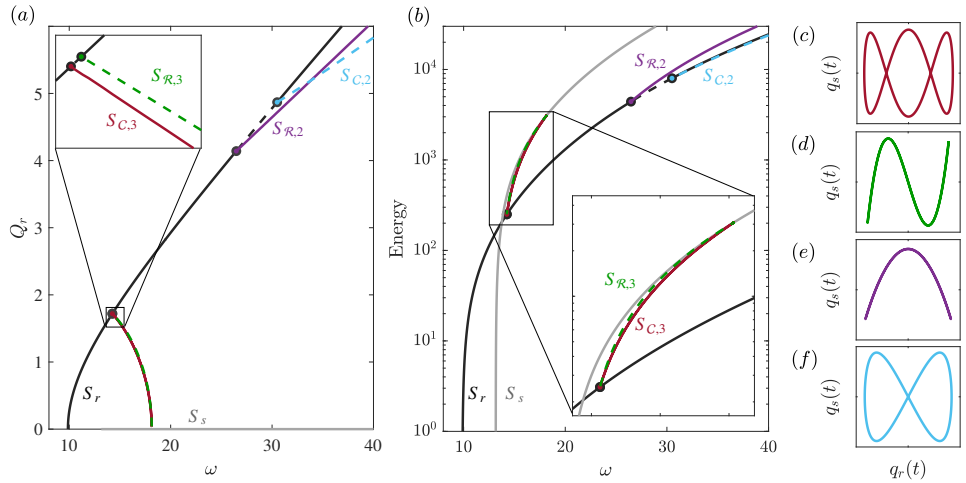

Figure 1. Internal resonances in a pinned-pinned beam with a two-mode truncation. Panel (a) shows the NNMs in the projection of response frequency, ω, against displacement amplitude of the first mode, Q_r; whilst panel (b) shows the NNMs in the frequency-energy projection. The grey line, labelled S_s, represents the primary backbone emerging from ω_{ns}, with response frequency divided by three to denote $1:3$ frequency commensurate relationship. The stable and unstable solutions are represented by solid and dashed lines respectively. Panels $(c) \sim (f)$ show the schematic time-parameterised responses, i.e. $q_r(t)$ against $q_s(t)$, of NNMs in panels (a) and (b). (Online version in colour.)

Table 1. Classification of NNMs by referring to Fourier components of q_r and q_s.

NNM type	Fourier components of q_r and q_s	Examples
Fourier-real NNM	q_r : real Fourier components; q_s : real Fourier components	figures 1d and 1e
Fourier-complex NNM	q_r : real Fourier components; q_s : complex Fourier components	figures 1c and 1f

also to capture its geometric features in the complex plane, we refer to the Fourier components of q_r and q_s. Here, we define an NNM where both q_r and q_s consist of real Fourier components (equivalently, consisting of only cosine components) as a Fourier-real NNM (a line in the time-parameterised space), e.g. panels (d) and (e); whilst a Fourier-complex NNM denotes the case where q_r is composed of real Fourier components and q_s is composed of complex Fourier components (a loop in the time-parameterised space), e.g. panels (c) and (f). The definitions are summarised in table 1. Note that, referring to Fourier components is equivalent to considering the phase relationships between two modes. Combining the commensurate frequency relationships and the phase relationships between the two modes, these four NNMs, in panels (c), (d), (e) and (f), can be uniquely termed $1:3$ Fourier-complex, $1:3$ Fourier-real, $1:2$ Fourier-real and $1:2$ Fourier-complex NNMs, respectively; and their corresponding branches are denoted by $S_{\mathcal{C},3}$, $S_{\mathcal{R},3}$, $S_{\mathcal{R},2}$ and $S_{\mathcal{C},2}$ in figure 1.

It is shown in figure 1a that the pitchfork bifurcations are either subcritical or supercritical [23], leading to unstable and stable mixed-mode NNM branches, respectively. Unlike the $1:2$ internal resonances where the two associated NNM branches are well-separated, the $1:3$ Fourier-real and -complex branches, $S_{\mathcal{R},3}$ and $S_{\mathcal{C},3}$, in this case, are almost indistinguishable in panels (a) and (b). To further study this case, evolutions of the bifurcation amplitudes with respect to $\Psi_{2,2}$ (with other parameters fixed) are shown in figure 2. As $\Psi_{2,2}$ increases, the response amplitudes of the bifurcations diverge, and two corresponding asymptotes can be observed, where the amplitudes become infinite. The limiting case of $\Psi_{2,2} \to +0$ denotes when the two bifurcations converge to an identical point with a finite value. As such, the coexistence of $S_{\mathcal{R},3}$ and $S_{\mathcal{C},3}$ can be observed

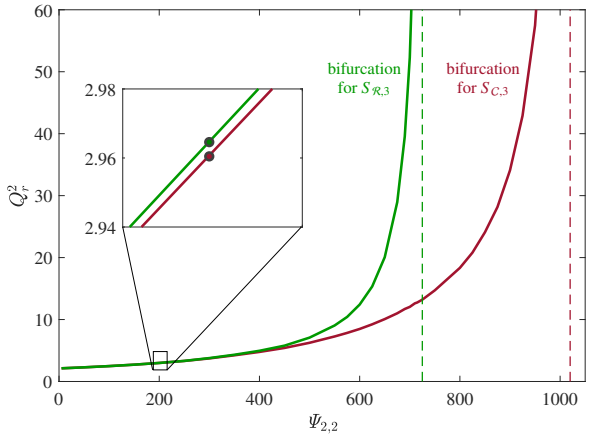

Figure 2. Evolutions of bifurcations that lead to $1:3$ Fourier-real and -complex NNMs, $S_{\mathcal{R},3}$ and $S_{\mathcal{C},3}$. The embedded plot presents the bifurcations for the two-mode beam system shown in figure 1. (Online version in colour.)

when $\Psi_{2,2}$ is below the values of asymptotes. Note that, the converging and diverging behaviours of bifurcations and NNMs will be revisted in §3. The two-mode beam case, studied above, has $\Psi_{2,2} = 2\pi^4$, and the bifurcations are marked by dots in the embedded plot of figure 2. Note that, in both figures 1 and 2, due to the similarity in amplitudes and response frequencies for $S_{\mathcal{R},3}$ and $S_{\mathcal{C},3}$, an extremely small step size is required in the numerical continuation to differentiate them. Such a refined step size can be considered analogous to accounting for harmonic effects in the analytical derivations. When only the fundamental components of the modes are considered in modal interactions, the two similar, yet independent, bifurcations, leading to $S_{\mathcal{R},3}$ and $S_{\mathcal{C},3}$, degenerate to a multiple root [5].

In practice, NNMs have proven to be an efficient tool for studying internal resonances in nonlinear systems [21,32,33]. To achieve this, a complete structure of NNMs is required; however, a particular computational effort and a prior knowledge may be needed if a purely numerical technique is used to determine the internal resonances, e.g. to distinguish the two solutions of $1:3$ internal resonances in the example two-mode beam system. In this study, we consider the existence and locations of internal resonances between two interacting modes with an arbitrary eigenfrequency ratio. A graphical method is also proposed for efficient determination/prediction of the internal resonances.

3. Existence and interpretation of internal resonances

In this section, we consider the general two-mode system whilst the specific two-mode beam case will be revisted to aid interpretation whenever necessary. Here, the symmetric case where $\Psi_{3,1} = \Psi_{1,3} = 0$ is first considered, this represents the case where a system has a symmetric layout/configuration[2] [5,29]. The effect of symmetry breaking, or invariant-breaking considered in [17], will be considered in §4.

With symmetry, the equations of motion (2.1) in the modal domain can be reduced to

$$\ddot{q}_r + \omega_{nr}^2 q_r + \Psi_{4,0} q_r^3 + \Psi_{2,2} q_r q_s^2 = 0\,, \tag{3.1a}$$

$$\ddot{q}_s + \omega_{ns}^2 q_s + \Psi_{2,2} q_r^2 q_s + \Psi_{0,4} q_s^3 = 0\,. \tag{3.1b}$$

Without loss of generality, we consider the scenario that internal resonances exist in the neighbourhood of S_r, i.e. the single-mode NNM branch that emerges from eigenfrequency ω_{nr}.

[2]Note that this is equivalent to having $Z_2 \oplus Z_2$ symmetry as discussed in [34].

As such, any internal resonance can be captured by an NNM in which q_r is the dominant mode and q_s is the mode with which it is resonating. In this case, q_s may be assumed to be small when compared with q_r, which allows q_s^2 and q_s^3 to be considered as higher-order small terms, $\mathcal{O}(q_s^2)$, hence equations (3.1) may be written

$$\ddot{q}_r + \omega_{nr}^2 q_r + \Psi_{4,0} q_r^3 + \mathcal{O}(q_s^2) = 0\,, \tag{3.2a}$$

$$\ddot{q}_s + \omega_{ns}^2 q_s + \Psi_{2,2} q_r^2 q_s + \mathcal{O}(q_s^2) = 0\,. \tag{3.2b}$$

Trivial solutions can be found when $q_r = q_s = 0$, corresponding to static equilibrium. Whilst, for non-trivial solutions, one case is related to $q_r \neq 0$ and $q_s = 0$, which describes the single-mode NNM branch, S_r. In this case, q_r can be expressed as a sum of harmonic components, i.e.

$$q_r = \sum_{m=0}^{\infty} Q_{r,m} \cos(m\omega t)\,. \tag{3.3}$$

Here, a single-harmonic approximation is first considered by assuming that $q_r \approx Q_{r,1}\cos(\omega t)$; and thus, this formulation is termed having a first-order of accuracy [35]. Using $q_s = 0$, equations (3.2) can be solved to give the approximate expression for S_r, i.e.

$$S_r(\omega, Q_{r,1}): \quad \omega^2 = \omega_{nr}^2 + \frac{3}{4}\Psi_{4,0} Q_{r,1}^2\,. \tag{3.4}$$

Another non-trivial solution set is related to $q_r \neq 0$ and $q_s \neq 0$, emerging from internal resonances. Ignoring the contributions from higher-order small terms, i.e. considering internal resonances in the neighbourhood of S_r, expressions for mixed-mode NNMs can be obtained by substituting solutions of q_r, i.e. $q_r \approx Q_{r,1}\cos(\omega t)$, into equation (3.2*b*). After some algebraic manipulation, the internal resonances can be captured by the Mathieu equation, given by

$$\frac{\partial^2 q_s}{\partial \tau^2} + [\delta + \epsilon\cos(\tau)]\, q_s = 0\,, \tag{3.5}$$

where

$$\tau = 2\omega t, \quad \delta = \frac{2\omega_{ns}^2 + \Psi_{2,2} Q_{r,1}^2}{8\omega^2} \quad \text{and} \quad \epsilon = \frac{\Psi_{2,2} Q_{r,1}^2}{8\omega^2}. \tag{3.6}$$

The equivalence between the internal resonances (of a first-order accuracy) and the Mathieu equation offers a novel perspective to understand internal resonances – dynamic responses in the internally resonant mode, q_s, triggered by the parametric forcing from the dominant mode, q_r. Seen from equation (3.5), with an assumed solution for q_r, the dynamics of q_s is entirely determined by the two parameters, δ and ϵ. These parameters are functions of ω and $Q_{r,1}$, and hence will vary for different responses on the single-mode NNM branch, S_r. To solve this equation, the response of q_s is approximated using a sum of harmonics, i.e.

$$\begin{aligned} q_s &= Q_{sa,0} + \sum_{n=1}^{\infty} Q_{sa,n}\cos(n\omega t) + Q_{sb,n}\sin(n\omega t) \\ &= Q_{sa,0} + \sum_{n=1}^{\infty} Q_{sa,n}\cos\left(\frac{n}{2}\tau\right) + Q_{sb,n}\sin\left(\frac{n}{2}\tau\right)\,. \end{aligned} \tag{3.7}$$

Substituting solutions (3.7) into equation (3.5), the harmonic components can be balanced to give four independent groups of equations [36], dealing with unknown variables, $Q_{sa,n}$ and $Q_{sb,n}$ respectively, with n denoting either even or odd non-negative integers, i.e.

$1:n$ Fourier-real NNMs for even n, $S_{\mathcal{R},n}$:

$$\begin{bmatrix} \delta & \epsilon/2 & 0 & \\ \epsilon & \delta-1 & \epsilon/2 & \cdots \\ 0 & \epsilon/2 & \delta-4 & \\ & \vdots & & \end{bmatrix} \begin{pmatrix} Q_{sa,0} \\ Q_{sa,2} \\ Q_{sa,4} \\ \vdots \end{pmatrix} = \mathbf{0}\,, \tag{3.8a}$$

$1:n$ Fourier-complex NNMs for even n, $S_{\mathcal{C},n}$:

$$\begin{bmatrix} \delta-1 & \epsilon/2 & 0 & \\ \epsilon/2 & \delta-4 & \epsilon/2 & \cdots \\ 0 & \epsilon/2 & \delta-9 & \\ & \vdots & & \end{bmatrix} \begin{pmatrix} Q_{sb,2} \\ Q_{sb,4} \\ Q_{sb,6} \\ \vdots \end{pmatrix} = \mathbf{0}\,, \tag{3.8b}$$

$1:n$ Fourier-real NNMs for odd n, $S_{\mathcal{R},n}$:

$$\begin{bmatrix} \delta-1/4+\epsilon/2 & \epsilon/2 & 0 & \\ \epsilon/2 & \delta-9/4 & \epsilon/2 & \cdots \\ 0 & \epsilon/2 & \delta-25/4 & \\ & \vdots & & \end{bmatrix} \begin{pmatrix} Q_{sa,1} \\ Q_{sa,3} \\ Q_{sa,5} \\ \vdots \end{pmatrix} = \mathbf{0}\,, \tag{3.8c}$$

$1:n$ Fourier-complex NNMs for odd n, $S_{\mathcal{C},n}$:

$$\begin{bmatrix} \delta-1/4-\epsilon/2 & \epsilon/2 & 0 & \\ \epsilon/2 & \delta-9/4 & \epsilon/2 & \cdots \\ 0 & \epsilon/2 & \delta-25/4 & \\ & \vdots & & \end{bmatrix} \begin{pmatrix} Q_{sb,1} \\ Q_{sb,3} \\ Q_{sb,5} \\ \vdots \end{pmatrix} = \mathbf{0}\,. \tag{3.8d}$$

Nontrivial solutions to these four equation sets capture internal resonances of the system. Considering equation set (3.8*a*) for example, any q_s solution is composed of a series of cosine components, whose response frequencies are even multiples of that of q_r. Recalling $q_r \approx Q_{r,1}\cos(\omega t)$, both q_r and q_s are composed of cosine components; thus, solutions to equation set (3.8*a*) are $1:n$ Fourier-real NNMs for even n, e.g. the $1:2$ Fourier-real NNM shown in figure 1*e*. Likewise, solutions to equation sets (3.8*b*), (3.8*c*) and (3.8*d*) denote $1:n$ Fourier-complex (even n), $1:n$ Fourier-real (odd n), and $1:n$ Fourier-complex (odd n) NNMs, respectively; corresponding examples are shown in panels (f), (d) and (c) of figure 1.

As discussed in previous sections, the existence of internal resonances is captured by NNM branches bifurcating from the primary branch via pitchfork bifurcations. To determine the stability-changing bifurcations, and the existence of internal resonances, the Hill's method is used [36]. The so-called Hill's method is formulated by constructing zero determinants of the four coefficient matrices in equations (3.8), termed Hill's determinants, which are also conditions to obtain non-trivial solutions. Using Hill's method in determining stability yields the same results as that by referring to Floquet exponents [37]. In figure 3, the stability boundaries are shown as coloured solid lines in the $(\delta,\ \epsilon)$ space, with the unstable regions shaded in colour. Using interpretations of the four equation sets (3.8), the stability boundaries are labelled with the types of bifurcated NNMs. This diagram is also termed the Ince-Strutt diagram, and has been widely used to study the stability of mechanical systems [38,39]. For the context considered in this paper, i.e. internal resonances between two modes, this diagram coincides with the formulation with a first-order of accuracy.

Using expressions (3.6), the single-mode NNM branch, given by equation (3.4), can be projected to the $(\delta,\ \epsilon)$ space as a straight line with a finite length, given by

$$S_r(\omega, Q_{r,1}) \mapsto S_r(\delta,\epsilon):\quad \epsilon = \frac{2\Psi_{2,2}\omega_{nr}^2}{2\Psi_{2,2}\omega_{nr}^2 - 3\Psi_{4,0}\omega_{ns}^2}\delta - \frac{\Psi_{2,2}\omega_{ns}^2}{2\left(2\Psi_{2,2}\omega_{nr}^2 - 3\Psi_{4,0}\omega_{ns}^2\right)}\,, \tag{3.9}$$

where

$$\delta \in \left[\frac{\omega_{ns}^2}{4\omega_{nr}^2},\ \frac{\Psi_{2,2}}{6\Psi_{4,0}}\right) \quad \text{and} \quad \epsilon \in \left[0,\ \frac{\Psi_{2,2}}{6\Psi_{4,0}}\right)\,. \tag{3.10}$$

That is, S_r originates at coordinate $\left(\frac{\omega_{ns}^2}{4\omega_{nr}^2},\ 0\right)$ with a zero amplitude at its eigenfrequency, and approaches the coordinate $\left(\frac{\Psi_{2,2}}{6\Psi_{4,0}},\ \frac{\Psi_{2,2}}{6\Psi_{4,0}}\right)$ as the response amplitude tends asymptotically

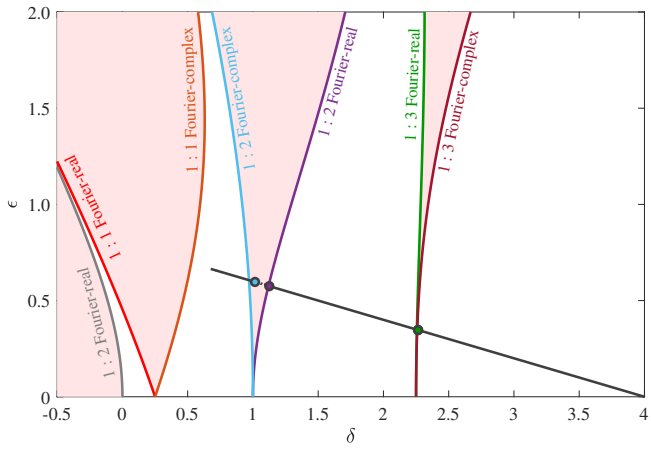

Figure 3. Determining the existence and locations of internal resonances. The boundaries, representative of collections of bifurcations on S_r for arbitrary systems, are labelled with types of the bifurcated NNMs. The first single-mode NNM branch for the pinned-pinned beam system, studied in §2, is projected as a straight line with a finite length via equation (3.9) with bifurcations denoted by solid dots. Note that the discrepancies between bifurcations and stability boundaries arise due to the fact that bifurcations are numerical solutions whilst the boundaries are computed with a first-order approximation via equation (3.8). (Online version in colour.)

towards infinity. Indeed, it is the asymptotic feature of the primary NNM that leads to asymptotic divergence of bifurcations, shown in figure 2; this will be revisted in the following discussions. In this space, the intersections between S_r and the boundaries represent bifurcations, leading to NNMs of the labelled types, along with stability changes on S_r. For example, the primary NNM branch of the two-mode beam system, considered in §2, is computed via numerical continuation and shown as a straight line with a finite length in figure 3. The bifurcations are marked by dots, which approximately lie on the boundaries, capturing the existence of internal resonances, observed in figure 1. This provides a graphical method for efficiently predicting the internal resonances that can be observed by checking the existing intersections. There are some small discrepancies between the numerically obtained bifurcations and the stability boundaries, especially at higher amplitudes. This is because the formulation of a first-order accuracy, presented here, only accounts for the fundamental component in q_r; whilst, as amplitude increases, the contributions from harmonics become more significant. To account for the harmonic contributions, the formulation with a higher-order approximation is derived in Appendix A, which results in an extended Mathieu equation and having an improved accuracy. As the essential topologies of internal resonances are captured by this first-order-accuracy formulation, the following discussions retain this formulation for simplicity. In the following, the existence of internal resonances are further investigated to understand their topological features.

(a) Topologies of internal resonances: the converging behaviour

In the $(\delta,\ \epsilon)$ space, figure 3, the $1:n$ Fourier-real and Fourier-complex stability boundaries exist as a pair, and those two boundaries share an identical solution for the limited case when $\epsilon \to +0$. The coalescence of the stability boundaries indicates the convergence of two bifurcations, as already observed with the limited condition when $\Psi_{2,2} \to +0$ in figure 2.

Taking the $1:3$ internal resonances as an example, the evolutions of bifurcations and correlated NNMs, $S_{\mathcal{R},3}$ and $S_{\mathcal{C},3}$, are shown with respect to a varied $\Psi_{2,2}$ in figure 4. Example cases are shown in panels (a) to (e) in the frequency-amplitude projection; schematic responses on the NNMs are shown in the time-parameterised space in the embedded plots. As with that in figure 2,

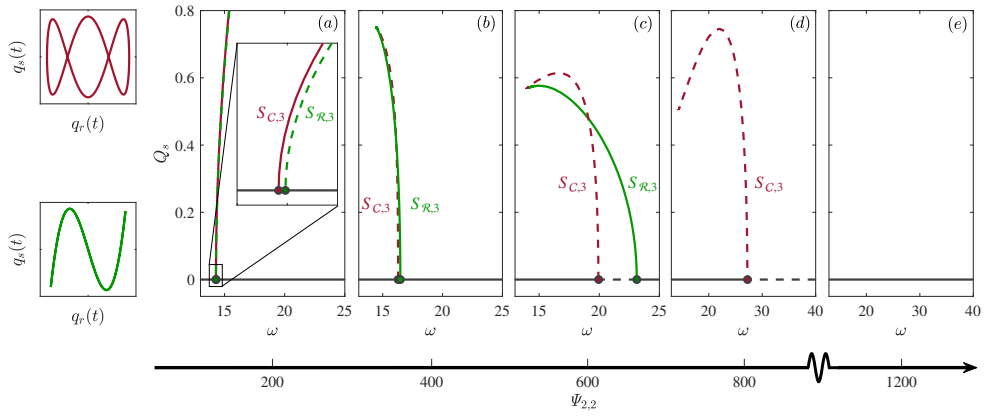

Figure 4. Convergence of bifurcations and mixed-mode NNMs. Panels (a) to (e) show evolutions of $S_{\mathcal{R},3}$ and $S_{\mathcal{C},3}$ for a two-mode system with $\omega_{ns}/\omega_{nr} = 4, \Psi_{4,0} = \pi^4/2$ and a varied $\Psi_{2,2}$, in the projection of response frequency, ω, against amplitude of q_s. The embedded plots show the schematic responses of the backbone curves in the time-parameterised space, i.e. $q_r(t)$ against $q_s(t)$. (Online version in colour.)

the decrement of $\Psi_{2,2}$ leads to the convergence of bifurcations. In addition, the two correlated mixed-mode NNM branches, $S_{\mathcal{R},3}$ and $S_{\mathcal{C},3}$, also converge, as shown in panels (a), (b) and (c). Considering the limited condition when $\Psi_{2,2} \to 0$, $S_{\mathcal{R},3}$ and $S_{\mathcal{C},3}$ share identical amplitudes and response frequencies – it can be derived analytically from equations (3.8*c*) and (3.8*d*), where these two associated solution sets converge to multiple roots when $\Psi_{2,2} \to 0$. However, these two solutions exhibit different Fourier components in q_s, as indicated by the subscripts of vector elements in equations (3.8*c*) and (3.8*d*); this is equivalent to having different phase relationships between q_r and q_s, as schematically shown in the $(q_r(t),\ q_s(t))$ space in figure 4. In this case, the $1:3$ internal resonances are captured by NNMs that exhibit undetermined phase relationships, which can be either Fourier-real or Fourier-complex. These undetermined phase relationships, or unlocked phase relationships, represent resonances that are rarely observed in the presence of forcing and damping [40]. This feature can also be directly observed from the equations of motion (3.1), which reduce to two uncoupled Duffing's oscillators when $\Psi_{2,2} \to 0$ (as $\Psi_{2,2}$ is the only coupling parameter for symmetric case). In this case, the converged solutions denote cases where the two modes vibrate independently rather than interactionally, yet with a constant response frequency ratio. Similar phenomena can be observed for other types of internal resonances. In contrast, as shown in figure 4, the increment of $\Psi_{2,2}$ leads to the divergence of bifurcations and their correlated mixed-mode NNMs, see panels (c), (d) and (e). This results in the annihilation of internal resonances, analysed in the following section.

(b) Topologies of internal resonances: topological divisions

As shown in figure 3, the primary NNM branch of the two-mode beam intersects with multiple boundary pairs, leading to $1:2$ and $1:3$ internal resonances. Such an intricate topology of internal resonances has been reported in other systems [21–23]. To determine the existence and types of internal resonances, discussions are further extended to consider the combined effect of multiple internal resonances for a general two-mode system. To facilitate the interpretations of internal resonance, the boundary pairs, shown in figure 3, are remapped from the $(\delta,\ \epsilon)$ space to the $\left(\Psi_{2,2}/\Psi_{4,0},\ Q_{r,1}^2\right)$ space. This allows the physical interpretations, namely the required system parameters and response amplitudes, of internal resonances to be directly determined from the

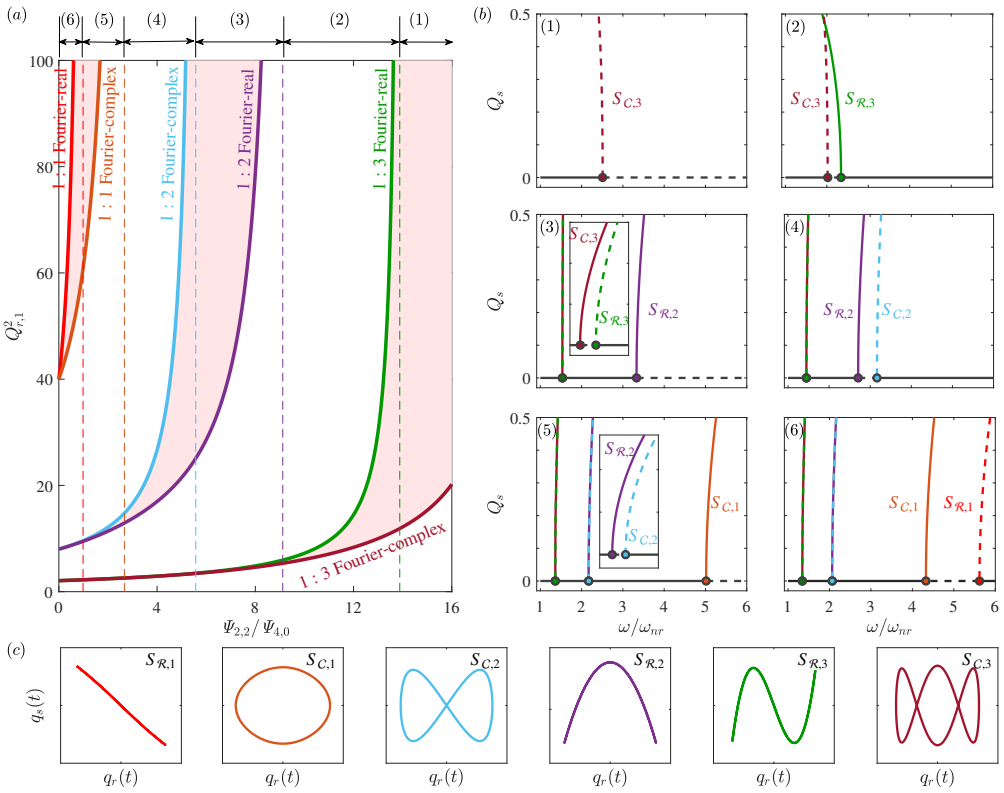

Figure 5. Topological evolutions of NNMs that bifurcate from the *first* single-mode NNM for a two-mode system with $\omega_{ns}/\omega_{nr} = 4$ and $\Psi_{4,0} = \pi^4/2$. Panel (a) shows the evolutions of bifurcation amplitudes with respect to a varied coefficient $\Psi_{2,2}/\Psi_{4,0}$. Asymptotes of the loci divide the space into six regions, $(1) \sim (6)$, capturing the topological changes of internal resonances. The topologies of NNMs for these regions are shown in panel (b). Panel (c) presents the schematic time-parameterised responses on the bifurcated NNM branches. (Online version in colour.)

mapping axes. Using expressions (3.4) and (3.6), the projection is defined as

$$(\delta,\ \epsilon) \mapsto (\Psi_{2,2}/\Psi_{4,0},\ Q^2_{r,1}) : \quad \frac{\Psi_{2,2}}{\Psi_{4,0}} = \frac{6\epsilon\omega^2_{ns}}{\omega^2_{ns} - 4\omega^2_{nr}\,(\delta - \epsilon)}\,,\ Q^2_{r,1} = \frac{4\,(\epsilon - \delta)\,\omega^2_{nr} + \omega^2_{ns}}{3\Psi_{4,0}\,(\delta - \epsilon)}\,. \tag{3.11}$$

First, the case where $\omega_{nr} < \omega_{ns}$ is considered to study the NNMs that bifurcate from the *first* primary NNM branch for a two-mode system. With $\omega_{ns}/\omega_{nr} = 4$ and $\Psi_{4,0} = \pi^4/2$, the results are shown in figure 5, where the remappings of the stability boundaries are shown in panel (a). It is shown that the bifurcations for $1:n$ Fourier-real and Fourier-complex NNMs converge with the decrement of $\Psi_{2,2}$, similar to the numerically obtained example in figure 2. In this projection, the primary single-mode NNM, S_r, for any system with determined $\Psi_{2,2}/\Psi_{4,0}$ is a vertical line; and as previously discussed, the intersections between the primary NNM and the boundaries indicate bifurcations that lead to mixed-mode NNMs of the labelled types. Example time-parameterised responses on these NNMs are shown in panel (c), where the commensurate frequency relationships can be checked – q_s (the mode with a *higher* eigenfrequency), is resonating at frequencies that are integer multiples of that of q_r (the mode with a *lower* eigenfrequency).

In figure 5*a*, it can be observed that each boundary has an asymptote, corresponding to a critical case where the bifurcation amplitude grows to infinity, when the correlated internal resonances become non-existent. As such, these asymptotes serve as boundaries for topological changes of bifurcations and their correlated internal resonances. The asymptotic values can be

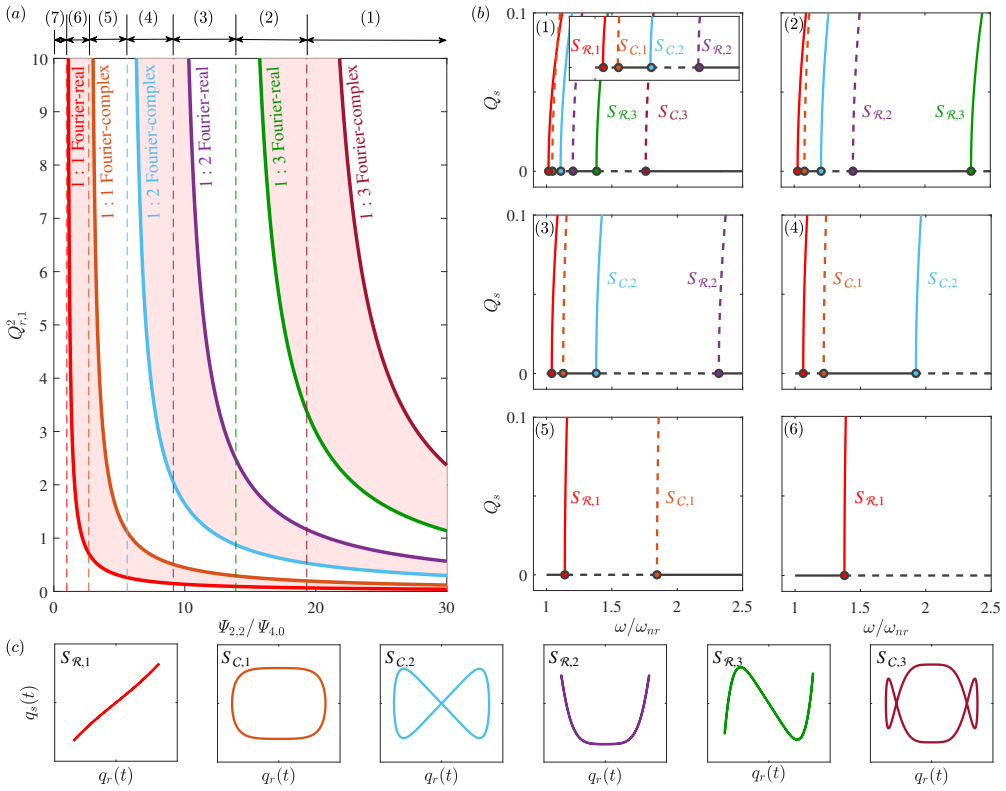

Figure 6. Topological evolutions of NNMs that bifurcate from the *second* single-mode NNM branch for a two-mode system with $\omega_{ns}/\omega_{nr} = 0.3$ and $\Psi_{4,0} = 1$. Panel (a) shows the evolutions of bifurcation amplitudes with respect to a varied coefficient $\Psi_{2,2}/\Psi_{4,0}$. Asymptotes of the loci divide the space into seven regions, $(1) \sim (7)$, where the topologies of NNMs in these regions are shown in panel (b). Panel (c) presents the schematic time-parameterised responses on bifurcated NNM branches. (Online version in colour.)

obtained by checking the Hill's determinants via mapping (3.11). Here, the asymptotic features are further investigated. Using these asymptotes, figure 5*a* can be divided into six regions[3], the corresponding topologies of NNMs are shown in panel (b) in the frequency-amplitude projection. In region (1), S_r only intersects with the stability boundary related to $S_{\mathcal{C},3}$, as such, the NNM topology (1) in panel (b) can be observed. Note that, for this case, $S_{\mathcal{C},3}$ is unstable due to the subcritical bifurcation. Moving from region (1) to region (2), the bifurcation, leading to $S_{\mathcal{R},3}$, merges from an infinite amplitude, and evolves to a lower amplitude as $\Psi_{2,2}/\Psi_{4,0}$ decreases. The topologies of NNMs, for systems in region (2), are shown in plot (2) of panel (b). Decreasing $\Psi_{2,2}/\Psi_{4,0}$ leads to region (3), where $S_{\mathcal{R},2}$ merges, and where the two bifurcations of $1:3$ internal resonances further converge to similar amplitudes. Likewise, further decreasing $\Psi_{2,2}/\Psi_{4,0}$ leads to the emergence of $S_{\mathcal{C},2}$, $S_{\mathcal{C},1}$ and $S_{\mathcal{R},1}$ in turn respectively. The topological evolutions of NNMs are shown in plots $(4 \sim 6)$ of panel (b). For small values of $\Psi_{2,2}/\Psi_{4,0}$, e.g. in region (6), the $1:2$ internal resonances, as well as $1:3$ resonances, exhibit almost identical amplitudes and response frequencies for the NNMs, see plot (6) in panel (b). A small step size in numerical continuation would be required to distinguish between them. Note that the two-mode beam system, considered in §2, has $\Psi_{2,2}/\Psi_{4,0} = 4$. Its first primary NNM branch lies in region (4), as such, $1:3$ and $1:2$ internal resonances are expected, with NNMs topologically shown in figure 5*b*(4), in line with numerical results in figure 1*a*.

[3]Unlike figure 3, where the projection is universal for any single-mode NNM branch, the divisions in figure 5*a* are particular for the parameters considered here. For a system with a different eigenfrequency ratio, different divisions may be found.

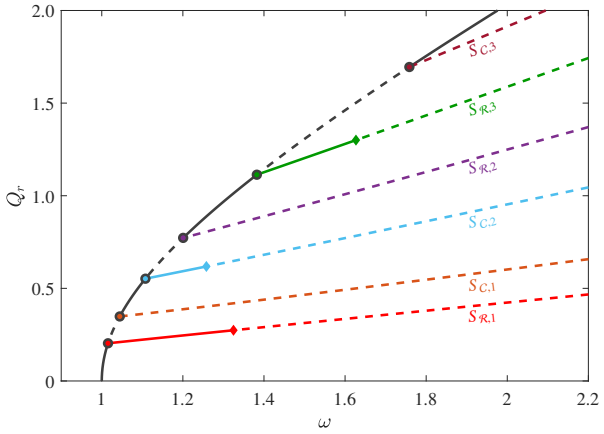

Figure 7. NNMs for a system with $\omega_{nr} = 1, \omega_{ns} = 0.3, \Psi_{2,2} = 30$ and $\Psi_{4,0} = 1$. The stable and unstable solutions are denoted by solid and dashed lines respectively. The pitchfork bifurcations on the primary NNM branch are marked by solid dots; whilst that on mixed-mode NNMs are marked by diamonds. (Online version in colour.)

So far, the existence and interpretations of internal resonances, in the neighbourhood of the first single-mode NNM branch, have been studied. It is also of interest to consider the scenarios on the *second* single-mode NNM branch in a two-mode system, i.e. cases where $\omega_{nr} > \omega_{ns}$. Figure 6 shows the topological evolutions of internal resonances for a system with $\omega_{ns}/\omega_{nr} = 0.3, \Psi_{4,0} = 1$ and a varied $\Psi_{2,2}$. As with the case in figure 5*a*, there is an asymptote for each stability boundary in panel (a), differentiating the topologies of NNMs, shown in panel (b), in the frequency-amplitude projection; whilst plots in panel (c) show the schematic time-parameterised responses on corresponding NNMs.

As with the cases considered in figure 5, q_s is resonating at frequencies that are integer multiples of that of q_r. Note that, in panel (c), some distortions can be observed in the responses due to the increment of amplitudes for different frequency components. In addition, in figure 6*a*, the stability boundaries converge as $\Psi_{2,2}$ increases (in comparison to the convergence as $\Psi_{2,2}$ decreases in figure 5*a*). As such, along the second single-mode NNM with an increased amplitude, the very first internal resonance to be observed is the $1:1$ Fourier-real type. This also results in a region where no internal resonance can be observed in the neighbourhood of the second single-mode NNM, see region (7) in panel (a) for systems with small $\Psi_{2,2}/\Psi_{4,0}$ values. Such a region with no internal resonance can be expected for all cases where $\omega_{nr} > \omega_{ns}$.

The NNMs for an example system with $\Psi_{2,2}/\Psi_{4,0} = 30$ are computed via numerical continuation and shown in figure 7. The stable and unstable solutions are denoted by solid and dashed lines respectively. The bifurcations on the primary NNM branch are marked by solid dots. As predicted in figure 6*a*, a series of mixed-mode NNMs, $S_{\mathcal{R},1}$, $S_{\mathcal{C},1}$, $S_{\mathcal{C},2}$, $S_{\mathcal{R},2}$, $S_{\mathcal{R},3}$ and $S_{\mathcal{C},3}$ can be observed. Note that, some pitchfork bifurcations, on the mixed-mode NNMs, are also detected and marked by diamonds. As these bifurcations are beyond the scope of this study, the bifurcated branches are not shown here.

In this section, the Fourier-real and Fourier-complex NNMs, defined in §2, are shown to exist as pairs – an extension of the special $1:1$ case studied in [4]. The converging behaviour of such a pair leads to uncoupled oscillators with phase-unlocked resonances – exact cases of that studied in [40]. Whilst the diverging behaviour of these pairs leads to the annihilation of internal resonances, and thus serving as their topological boundaries. For a particular two-mode system with an arbitrary eigenfrequency ratio, a finite number of internal resonances can be determined by checking the intersections between the primary NNM branch and boundaries. Besides determining the existence and locations, topological features of internal resonances

can be studied via this technique, e.g. the first mixed-mode NNM that bifurcates from the higher-natural-frequency primary NNM, as amplitude increases, is the $1:1$ Fourier-real type.

4. Effect of symmetry breaking on internal resonances

Up to this point, the discussion has centred around symmetric systems. In practice, asymmetry can be widely observed in mechanical systems, for example, asymmetry can arise due to the imperfection of pinned-pinned beams [7,40]. When asymmetry is taken into account, i.e. $\Psi_{3,1} \neq 0$ and $\Psi_{1,3} \neq 0$, single-mode solutions with either $q_s = 0$ or $q_r = 0$ are no longer obtainable for equations of motion (2.1), whilst only solutions with both modal components can be found. Such mixed-mode solutions can arise due to two coupling mechanisms – one is the dynamic coupling considered in previous sections, where the interactions between q_r and q_s lead to internal resonances; the other one corresponds to quasi-static coupling, where the behaviour of a mode is dictated by the other [41–43]. To account for both quasi-static and dynamic coupling, q_s is defined as a combination of a quasi-static component, g (dictated by q_r), and a dynamic component, h (capturing the internally resonant components), given by

$$q_s = g(q_r) + h\,. \tag{4.1}$$

In this representation, internal resonances are referring to dynamic interactions between q_r and h. As defined in [42], the quasi-static function, g, represents a solution of

$$\omega_{ns}^2 g + \Psi_{3,1} q_r^3 + \Psi_{2,2} q_r^2 g + 3\Psi_{1,3} q_r g^2 + \Psi_{0,4} g^3 = 0\,, \tag{4.2}$$

equivalent to a static solution of q_s to equation (2.1*b*). Note that, alternative methods, e.g. the centre manifold theorem [44] or the normal form method [45] can be used to analyse the aymmetric case. Here, the solution (4.1) is employed to extend discussions to weakly asymmetric case rather than provide a complete overview of the asymmetric case. Such a formulation also allows connections to be established to obtain comparisons between the asymmetric case and the symmetric case considered in previous discussions.

The Lagrangian of the system is still given by equation (2.2). Replacing $q_s = g(q_r) + h$, and applying the Euler-Lagrange equation to expression (2.2), the equations of motion can be obtained with respect to unknown variables q_r and h, given by

$$\left[\left(\frac{\partial g}{\partial q_r}\right)^2 + 1\right]\ddot{q}_r + \frac{\partial g}{\partial q_r}\frac{\partial^2 g}{\partial q_r^2}\dot{q}_r^2 + \frac{\partial g}{\partial q_r}\ddot{h} + f_r + \frac{\partial g}{\partial q_r} f_s = 0\,, \tag{4.3a}$$

$$\ddot{h} + \frac{\partial^2 g}{\partial q_r^2}\dot{q}_r^2 + \frac{\partial g}{\partial q_r}\ddot{q}_r + f_s = 0\,, \tag{4.3b}$$

where

$$\begin{aligned} f_r &= \omega_{nr}^2 q_r + \Psi_{4,0} q_r^3 + 3\Psi_{3,1} q_r^2 (g+h) + \Psi_{2,2} q_r (g+h)^2 + \Psi_{1,3} (g+h)^3\,, \\ f_s &= \omega_{ns}^2 (g+h) + \Psi_{3,1} q_r^3 + \Psi_{2,2} q_r^2 (g+h) + 3\Psi_{1,3} q_r (g+h)^2 + \Psi_{0,4} (g+h)^3\,. \end{aligned}$$

This model was proposed in [46] to predict internal resonances, between q_r and h, during reduced-order modelling. As with discussions in §3, the internally resonant component, h, may be assumed to be small when compared with the dominant mode, q_r. Ignoring the higher-order small terms, $\mathcal{O}(h^2)$, the quasi-static coupling between q_r and q_s can be captured by equation (4.3*a*) and interpreted as a primary NNM branch containing the modal component q_r and quasi-statically coupled component $g(q_r)$. Whilst the internal resonances between q_r and h is captured by equation (4.3*b*). This is equivalent to considering internal resonances in the neighbourhood of the primary NNM branch; for details of this derivation please see [46].

Firstly, the quasi-static coupling function is solved via equation (4.2), where $g(q_r)$ is approximated by a Taylor series up to a cubic order[4], i.e.

$$g(q_r) \approx -\frac{\Psi_{3,1} q_r^3}{\omega_{ns}^2} \,. \tag{4.4}$$

Expression (4.4) shows how asymmetry, $\Psi_{3,1} \neq 0$, leads to quasi-static coupling. Combining expressions (4.2), (4.3*b*) and (4.4), and ignoring the effect of higher-order small terms, one has

$$\ddot{h} + \left(\omega_{ns}^2 + \Psi_{2,2} q_r^2 - \frac{6\Psi_{1,3}\Psi_{3,1}}{\omega_{ns}^2} q_r^4 + \frac{3\Psi_{0,4}\Psi_{3,1}^2}{\omega_{ns}^4} q_r^6\right) h = \frac{6\Psi_{3,1}}{\omega_{ns}^2} q_r \dot{q}_r^2 + \frac{3\Psi_{3,1}}{\omega_{ns}^2} q_r^2 \ddot{q}_r \,. \tag{4.5}$$

In the neighbourhood of the primary NNM branch, the solution for q_r is, as previous discussions, approximated using a single-harmonic component, $q_r \approx Q_{r,1}\cos(\omega t)$, i.e. having a first-order of accuracy. Substituting q_r back to equation (4.5), it can be simplified to

$$\frac{\partial^2 h}{\partial \tau^2} + \left[\delta_0 + \epsilon_1 \cos(\tau) + \epsilon_2 \cos(2\tau) + \epsilon_3 \cos(3\tau)\right] h = P_1 \left[\cos\left(\frac{1}{2}\tau\right) + 3\cos\left(\frac{3}{2}\tau\right)\right] , \tag{4.6}$$

where

$$\begin{aligned}
\delta_0 &= \frac{\omega_{ns}^2}{4\omega^2} + \frac{\Psi_{2,2}}{8\omega^2} Q_{r,1}^2 - \frac{9\Psi_{1,3}\Psi_{3,1}}{16\omega^2\omega_{ns}^2} Q_{r,1}^4 + \frac{15\Psi_{3,1}^2\Psi_{0,4}}{64\omega^2\omega_{ns}^4} Q_{r,1}^6 \,, \\
\epsilon_1 &= \frac{\Psi_{2,2}}{8\omega^2} Q_{r,1}^2 - \frac{3\Psi_{1,3}\Psi_{3,1}}{4\omega^2\omega_{ns}^2} Q_{r,1}^4 + \frac{45\Psi_{3,1}^2\Psi_{0,4}}{128\omega^2\omega_{ns}^4} Q_{r,1}^6 \,, \\
\epsilon_2 &= -\frac{3\Psi_{1,3}\Psi_{3,1}}{16\omega^2\omega_{ns}^2} Q_{r,1}^4 + \frac{9\Psi_{3,1}^2\Psi_{0,4}}{64\omega^2\omega_{ns}^4} Q_{r,1}^6 \,, \\
\epsilon_3 &= \frac{3\Psi_{3,1}^2\Psi_{0,4}}{128\omega^2\omega_{ns}^4} Q_{r,1}^6 \,, \\
P_1 &= -\frac{3\Psi_{3,1} Q_{r,1}^3}{16\omega_{ns}^2} \,.
\end{aligned}$$

This represents a nonhomogeneous extended Mathieu equation with two additional terms (characterised by coefficients ϵ_2 and ϵ_3). Here, h is approximated via a sum of harmonics, i.e.

$$h = H_{a,0} + \sum_{n=1}^{\infty} H_{a,n} \cos\left(\frac{n}{2}\tau\right) + H_{b,n} \sin\left(\frac{n}{2}\tau\right) \,. \tag{4.7}$$

Applying harmonic balancing, the mixed-mode NNMs, emerging from internal resonances in the neighbourhood of the primary NNM branch, can be obtained, given by

$1:n$ Fourier-real NNMs for even n, $S_{\mathcal{R},n}$:

$$\begin{bmatrix} \delta_0 & \epsilon_1/2 & \epsilon_2/2 & \\ \epsilon_1 & \delta_0 - 1 + \epsilon_2/2 & (\epsilon_1+\epsilon_3)/2 & \cdots \\ \epsilon_2 & (\epsilon_1+\epsilon_3)/2 & \delta_0 - 4 & \\ & \vdots & & \end{bmatrix} \begin{pmatrix} H_{a,0} \\ H_{a,2} \\ H_{a,4} \\ \vdots \end{pmatrix} = \mathbf{0} \,, \tag{4.8a}$$

$1:n$ Fourier-complex NNMs for even n, $S_{\mathcal{C},n}$:

$$\begin{bmatrix} \delta_0 - 1 - \epsilon_2/2 & (\epsilon_1-\epsilon_3)/2 & \epsilon_2/2 & \\ (\epsilon_1-\epsilon_3)/2 & \delta_0 - 4 & \epsilon_1/2 & \cdots \\ \epsilon_2/2 & \epsilon_1/2 & \delta_0 - 9 & \\ & \vdots & & \end{bmatrix} \begin{pmatrix} H_{b,2} \\ H_{b,4} \\ H_{b,6} \\ \vdots \end{pmatrix} = \mathbf{0} \,, \tag{4.8b}$$

[4]The same conclusions can be obtained when considering additional higher-order terms in the Taylor series, as such, a cubic approximation is considered for simplicity.

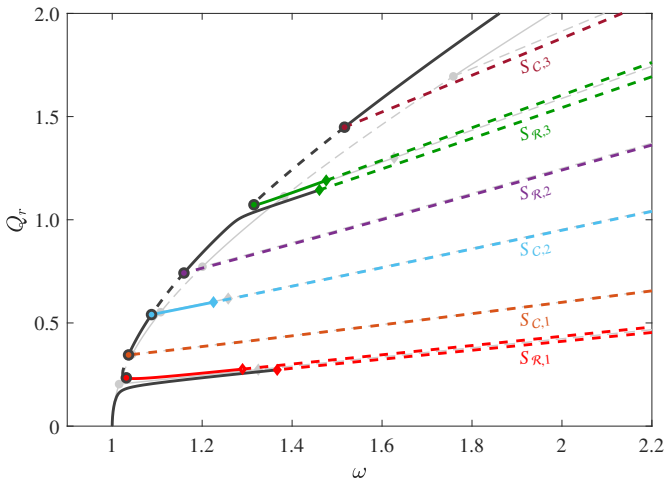

Figure 8. Effect of symmetry breaking on internal resonances. This plot presents NNMs for an asymmetric example system with $\omega_{nr} = 1$, $\omega_{ns} = 0.3$, $\Psi_{3,1} = 1.5$, $\Psi_{2,2} = 30$ and $\Psi_{4,0} = 1$. NNMs for the symmetric case, where $\Psi_{3,1} = 0$, are shown as thin grey lines for comparison. (Online version in colour.)

$1:n$ Fourier-real NNMs for odd n, $S_{\mathcal{R},n}$:

$$\begin{bmatrix} \delta_0 - 1/4 + \epsilon_1/2 & (\epsilon_1+\epsilon_2)/2 & (\epsilon_2+\epsilon_3)/2 & \cdots \\ (\epsilon_1+\epsilon_2)/2 & \delta_0 - 9/4 + \epsilon_3/2 & \epsilon_1/2 & \\ (\epsilon_2+\epsilon_3)/2 & \epsilon_1/2 & \delta_0 - 25/4 & \\ & \vdots & & \end{bmatrix} \begin{pmatrix} H_{a,1} \\ H_{a,3} \\ H_{a,5} \\ \vdots \end{pmatrix} = \begin{pmatrix} P_1 \\ 3P_1 \\ 0 \\ \vdots \end{pmatrix}, \tag{4.8c}$$

$1:n$ Fourier-complex NNMs for odd n, $S_{\mathcal{C},n}$:

$$\begin{bmatrix} \delta_0 - 1/4 - \epsilon_1/2 & (\epsilon_1-\epsilon_2)/2 & (\epsilon_2-\epsilon_3)/2 & \cdots \\ (\epsilon_1-\epsilon_2)/2 & \delta_0 - 9/4 - \epsilon_3/2 & \epsilon_1/2 & \\ (\epsilon_2-\epsilon_3)/2 & \epsilon_1/2 & \delta_0 - 25/4 & \\ & \vdots & & \end{bmatrix} \begin{pmatrix} H_{b,1} \\ H_{b,3} \\ H_{b,5} \\ \vdots \end{pmatrix} = \mathbf{0}\,. \tag{4.8d}$$

Solutions of these four equation sets represent asymmetric evolutions to that described by expressions (3.8). Except for equation set (4.8*c*), others remain as homogeneous equation sets. As such, semi-trivial solutions can be obtained for $S_{\mathcal{R},n}$ and $S_{\mathcal{C},n}$ for even n, and $S_{\mathcal{C},n}$ for odd n, determined by equations (4.8*a*), (4.8*b*) and (4.8*d*) respectively. This indicates these three mixed-mode NNMs remain bifurcating from the primary NNM branch via bifurcations. As for equation set (4.8*c*), only non-trivial solutions can be obtained due to nonhomogeneous terms on the right-hand side, indicating mixed-mode NNMs related to unfolded, or imperfect, bifurcations. This demonstrates the effect of symmetry breaking, arising from a cubic nonlinearity, on the internal resonances – it splits the bifurcations that lead to $S_{\mathcal{R},n}$ for odd n. Likewise, if the asymmetry is induced by nonlinear terms that have q_r with an even valued exponent, e.g. a quadratic nonlinearity, the bifurcations of $S_{\mathcal{R},n}$ for even n are unfolded; whilst the other three types remain bifurcating from the primary NNM branch. As with discussions in §3, the stability boundaries, for asymmetric cases, can be determined by the Hill's determinants for equations (4.8). It results in four-dimensional stability boundaries in the $(\delta_0, \epsilon_1, \epsilon_2, \epsilon_3)$ space.

Symmetry breaking is introduced to the example system shown in figure 7 by considering $\Psi_{3,1} = 1.5$. The asymmetric evolutions of the NNMs are computed via numerical continuation and shown in figure 8, where the NNMs for the symmetric case are denoted via thin grey lines for

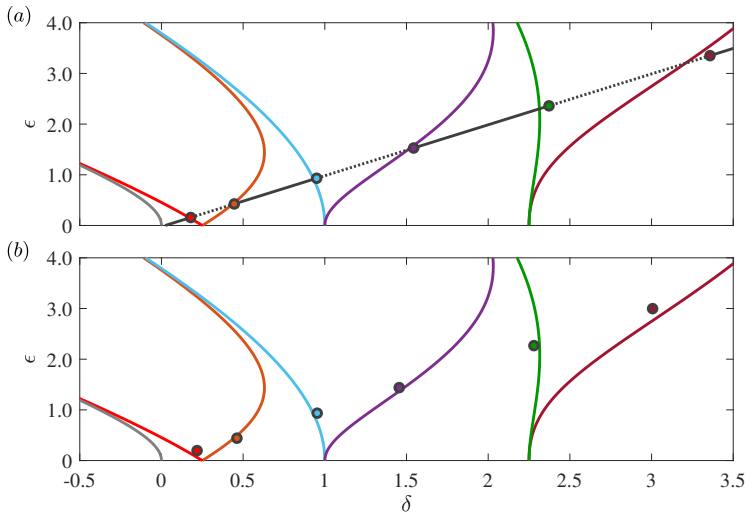

Figure 9. Existence and locations of internal resonances for an asymmetric system. Panel (a) shows the primary NNM branch in figure 7 (symmetric case), projected as a straight line with a finite length, whose bifurcations are marked by solid dots. Panel (b) shows the asymmetric evolutions of these bifurcations with $\Psi_{3,1} = 1.5$. (Online version in colour.)

comparison. It can be observed in breaking the symmetry two of the bifurcations, those leading to $S_{\mathcal{R},1}$ and $S_{\mathcal{R},3}$ have become imperfect bifurcations; whereas all the other bifurcations remain perfect, as also indicated by equations (4.8).

Another particular case of interest is when the system is seen as a small perturbation from the symmetric case. In this case, the symmetry-breaking parameters, $\Psi_{3,1}$ and $\Psi_{1,3}$, may be assumed as small terms. As such, ignoring the higher-order small terms in expression (4.6), it can be further simplified to

$$\frac{\partial^2 h}{\partial \tau^2} + [\delta + \epsilon \cos(\tau)]\, h = P_1 \left[\cos\left(\frac{1}{2}\tau\right) + 3\cos\left(\frac{3}{2}\tau\right)\right], \tag{4.9}$$

which represents a nonhomogeneous Mathieu equation, with left-hand side terms the same as that for symmetric case, considered in §3. The formation of expression (4.9) indicates that an asymmetric perturbation is equivalent to a nonhomogeneous perturbation to the internal resonances for a symmetric case; and it leads to bifurcation splitting, the same as elaborations of equations (4.8). In addition, as the frequencies of the nonhomogeneous terms are half integers to that on the left-hand side, there is no difference in the stability charts between the homogeneous and nonhomogeneous Mathieu equation [47]. This means the stability boundaries, shown in figure 3 for symmetric case, can be used to evaluate near-symmetric cases.

In figure 9a, the primary NNM branch in figure 7 (for a symmetric system) is projected to the $(\delta,\ \epsilon)$ space via expression (3.9) as a straight line. The bifurcations, leading to mixed-mode NNMs, are marked by solid dots, which approximately lie on the stability boundaries. The asymmetric evolutions of these bifurcations are also projected to this space in panel (b) for the system whose NNMs are shown in figure 8. There are some discrepancies between the numerically obtained bifurcations and the stability boundaries due to the formulation of a first-order accuracy. This can be addressed by referring to the formula of a higher-level accuracy, given in Appendix A.

5. Conclusion

Nonlinear coupling can give rise to rich dynamic phenomena, among which the internal resonance is an important feature. This work has considered the existence and locations of internal resonances for a two-mode system with an arbitrary eigenfrequency ratio.

This study starts with a general symmetric system, and it has been shown that the internal resonances can be approximately captured by the Mathieu equation. The associated bifurcations exist in pairs, leading to mixed-mode NNMs with the same commensurate frequency relationship but different phase relationships. Considering the topological evolutions of such pairs of bifurcations, the convergence of a pair leads to uncoupled oscillators with phase-unlocked resonances; whereas their divergence leads to the annihilation of internal resonances. Using these insights, a finite number of internal resonances can be determined; in addition, their topological features have been studied and explained, e.g. it has been shown that, as amplitude increases, the first mixed-mode NNM that bifurcates from the higher-natural-frequency primary NNM branch is the $1:1$ Fourier-real type.

The study then extends to asymmetric cases to account for the effect of symmetry breaking on internal resonances. Analytical derivations have shown that the unfolded bifurcations are captured by the non-homogeneous components of an extended Mathieu equation; whilst the remaining bifurcations are related to homogeneous components.

By exploring the existence and locations of internal resonances, this study provides an understanding of the mechanism underpinning internal resonances. A graphical method has also proposed for efficient determination and interpretation of internal resonances.

Data Accessibility. This article has no additional data.

Authors' Contributions. D.H. led the development of the work, with supervisory support from T.L.H. and S.A.N. All authors contributed to the preparation of the manuscript.

Funding. S.A.N is supported by an EPSRC Programme grant (EP/R006768/1) and D.H is supported by a scholarship from the CSC.

Acknowledgements. We gratefully acknowledge the financial support of the EPSRC and CSC.

A. Internal resonances with a second-order accuracy

In this Appendix, a formulation considering two harmonics in q_r is derived (termed as having a second-order-accuracy [35]) to study the internal resonances between q_r and q_s. Its accuracy is then compared with the first-order formulation, given in §3.

Accounting for the first and third harmonics, q_r is given by

$$q_r = Q_{r,1}\cos(\omega t) + Q_{r,3}\cos(3\omega t), \tag{A.1}$$

where response amplitude $Q_{r,3}$ may be assumed to be small when compared with $Q_{r,1}$. Substituting expression (A.1) into equation (3.2*b*), the mixed-mode NNMs in the neighbourhood of S_r are given by

$$\frac{\partial^2 q_s}{\partial \tau^2} + \left[\tilde{\delta} + \tilde{\epsilon}_1\cos(\tau) + \tilde{\epsilon}_2\cos(2\tau)\right] q_s = 0, \tag{A.2}$$

where

$$\tau = 2\omega t,\quad \tilde{\delta} = \frac{2\omega_{ns}^2 + \Psi_{2,2}Q_{r,1}^2}{8\omega^2},\quad \tilde{\epsilon}_1 = \frac{\Psi_{2,2}\left(Q_{r,1}^2 + 2Q_{r,1}Q_{r,3}\right)}{8\omega^2}\ \text{and}\ \tilde{\epsilon}_2 = \frac{\Psi_{2,2}Q_{r,1}Q_{r,3}}{4\omega^2}, \tag{A.3}$$

and where the contributions from higher-order small terms, $\mathcal{O}(q_2^2)$ and $\mathcal{O}(Q_{r,3}^2)$, are ignored. Compared with equation (3.5), equation (A.2) represents an extended Mathieu equation with an additional term characterised by coefficient $\tilde{\epsilon}_2$. To determine the mixed-mode solutions for equation (A.2), harmonic balance technique is again used. Assuming q_2 as a sum of harmonic components, i.e. expression (3.7), the obtained equation sets are given by

$1:n$ Fourier-real NNMs for even n, $S_{\mathcal{R},n}$:

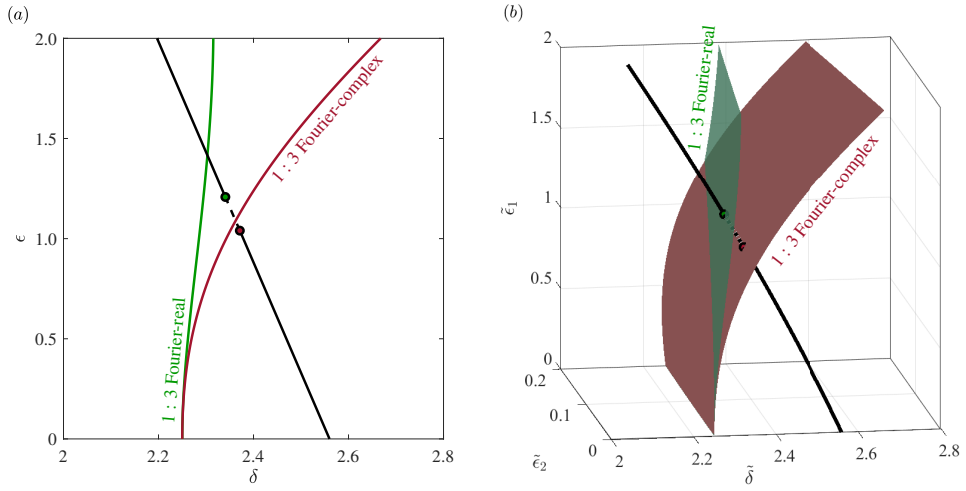

Figure 10. Comparing the predicted $1:3$ internal resonances using formulations of a first-order accuracy (panel (a)) and a second-order accuracy (panel (b)) for a system with $\omega_{nr}=1$, $\omega_{ns}=3.2$, $\Psi_{2,2}=13$ and $\Psi_{4,0}=1$. (Online version in colour.)

$$\begin{bmatrix} \tilde{\delta} & \tilde{\epsilon}_1/2 & \tilde{\epsilon}_2/2 & 0 & \\ \tilde{\epsilon}_1 & \tilde{\delta}-1+\tilde{\epsilon}_2/2 & \tilde{\epsilon}_1/2 & \tilde{\epsilon}_2/2 & \cdots \\ \tilde{\epsilon}_2 & \tilde{\epsilon}_1/2 & \tilde{\delta}-4 & \tilde{\epsilon}_1/2 & \\ 0 & \tilde{\epsilon}_2/2 & \tilde{\epsilon}_1/2 & \tilde{\delta}-9 & \\ & & \vdots & & \end{bmatrix} \begin{pmatrix} Q_{sa,0} \\ Q_{sa,2} \\ Q_{sa,4} \\ Q_{sa,6} \\ \vdots \end{pmatrix} = \mathbf{0}, \tag{A.4a}$$

$1:n$ Fourier-complex NNMs for even n, $S_{\mathcal{C},n}$:

$$\begin{bmatrix} \tilde{\delta}-1-\tilde{\epsilon}_2/2 & \tilde{\epsilon}_1/2 & \tilde{\epsilon}_2/2 & 0 & \\ \tilde{\epsilon}_1/2 & \tilde{\delta}-4 & \tilde{\epsilon}_1/2 & \tilde{\epsilon}_2/2 & \cdots \\ \tilde{\epsilon}_2/2 & \tilde{\epsilon}_1/2 & \tilde{\delta}-9 & \tilde{\epsilon}_1/2 & \\ 0 & \tilde{\epsilon}_2/2 & \tilde{\epsilon}_1/2 & \tilde{\delta}-16 & \\ & & \vdots & & \end{bmatrix} \begin{pmatrix} Q_{sb,2} \\ Q_{sb,4} \\ Q_{sb,6} \\ Q_{sb,8} \\ \vdots \end{pmatrix} = \mathbf{0}, \tag{A.4b}$$

$1:n$ Fourier-real NNMs for odd n, $S_{\mathcal{R},n}$:

$$\begin{bmatrix} \tilde{\delta}-1/4+\tilde{\epsilon}_1/2 & (\tilde{\epsilon}_1+\tilde{\epsilon}_2)/2 & \tilde{\epsilon}_2/2 & 0 & \\ (\tilde{\epsilon}_1+\tilde{\epsilon}_2)/2 & \tilde{\delta}-9/4 & \tilde{\epsilon}_1/2 & \tilde{\epsilon}_2/2 & \cdots \\ \tilde{\epsilon}_2/2 & \tilde{\epsilon}_1/2 & \tilde{\delta}-25/4 & \tilde{\epsilon}_1/2 & \\ 0 & \tilde{\epsilon}_2/2 & \tilde{\epsilon}_1/2 & \tilde{\delta}-49/4 & \\ & & \vdots & & \end{bmatrix} \begin{pmatrix} Q_{sa,1} \\ Q_{sa,3} \\ Q_{sa,5} \\ Q_{sa,7} \\ \vdots \end{pmatrix} = \mathbf{0}, \tag{A.4c}$$

$1:n$ Fourier-complex NNMs for odd n, $S_{\mathcal{C},n}$:

$$\begin{bmatrix} \tilde{\delta}-1/4-\tilde{\epsilon}_1/2 & (\tilde{\epsilon}_1-\tilde{\epsilon}_2)/2 & \tilde{\epsilon}_2/2 & 0 & \\ (\tilde{\epsilon}_1-\tilde{\epsilon}_2)/2 & \tilde{\delta}-9/4 & \tilde{\epsilon}_1/2 & \tilde{\epsilon}_2/2 & \cdots \\ \tilde{\epsilon}_2/2 & \tilde{\epsilon}_1/2 & \tilde{\delta}-25/4 & \tilde{\epsilon}_1/2 & \\ 0 & \tilde{\epsilon}_2/2 & \tilde{\epsilon}_1/2 & \tilde{\delta}-49/4 & \\ & & \vdots & & \end{bmatrix} \begin{pmatrix} Q_{sb,1} \\ Q_{sb,3} \\ Q_{sb,5} \\ Q_{sb,7} \\ \vdots \end{pmatrix} = \mathbf{0}. \tag{A.4d}$$

Using Hill's determinants, the stability boundaries can be computed in the $(\tilde{\delta},\ \tilde{\epsilon}_1,\ \tilde{\epsilon}_2)$ space. In this space, any primary NNM branch is a three dimensional line with a finite length, whose

intersections with the boundaries denote bifurcations, leading to labelled NNMs. An example is shown in figure 10*b*, which clearly shows an improved accuracy when compared with the formula of a first-order accuracy, derived in §3 and shown in panel (a) for comparison.

References

1. Nayfeh AH, Mook DT, Holmes P. 1980 Nonlinear oscillations. .
2. Glendinning P. 1994 *Stability, instability and chaos: an introduction to the theory of nonlinear differential equations* vol. 11. Cambridge university press.
3. Macdonald J. 2016 Multi-modal vibration amplitudes of taut inclined cables due to direct and/or parametric excitation. *Journal of Sound and Vibration* **363**, 473–494.
4. Hong D, Nicolaidou E, Hill TL, Neild SA. 2020 Identifying phase-varying periodic behaviour in conservative nonlinear systems. *Proceedings of the Royal Society A: Mathematical, Physical and Engineering Sciences* **476**, 20200028.
5. Lewandowski R. 1994 Solutions with bifurcation points for free vibration of beams: an analytical approach. *Journal of sound and vibration* **177**, 239–249.
6. Lewandowski R. 1996 On beams membranes and plates vibration backbone curves in cases of internal resonance. *Meccanica* **31**, 323–346.
7. Lacarbonara W, Arafat HN, Nayfeh AH. 2005 Non-linear interactions in imperfect beams at veering. *International Journal of Non-Linear Mechanics* **40**, 987–1003.
8. Emam SA, Nayfeh AH. 2013 Non-linear response of buckled beams to 1:1 and 3:1 internal resonances. *International Journal of Non-Linear Mechanics* **52**, 12–25.
9. Thomas O, Touzé C, Chaigne A. 2005 Non-linear vibrations of free-edge thin spherical shells: modal interaction rules and 1: 1: 2 internal resonance. *International Journal of Solids and Structures* **42**, 3339–3373.
10. Vakakis AF, Gendelman OV, Bergman LA, McFarland DM, Kerschen G, Lee YS. 2008 *Nonlinear targeted energy transfer in mechanical and structural systems* vol. 156. Springer Science & Business Media.
11. Kerschen G, Lee YS, Vakakis AF, McFarland DM, Bergman LA. 2005 Irreversible passive energy transfer in coupled oscillators with essential nonlinearity. *SIAM Journal on Applied Mathematics* **66**, 648–679.
12. Hong D, Hill TL, Neild SA. 2021 Understanding targeted energy transfer from a symmetry breaking perspective. *Proceedings of the Royal Society A: Mathematical, Physical and Engineering Sciences* **477**, 20210045.
13. Chen LQ, Jiang WA. 2015 Internal resonance energy harvesting. *Journal of Applied Mechanics* **82**.
14. Cao D, Leadenham S, Erturk A. 2015 Internal resonance for nonlinear vibration energy harvesting. *The European Physical Journal Special Topics* **224**, 2867–2880.
15. Nayfeh AH, Balachandran B. 1989 Modal interactions in dynamical and structural systems. *Applied Mechanics Reviews* **42**, S175–S201.
16. Manevich AI, Manevitch LI. 2005 *The Mechanics of Nonlinear Systems with Internal Resonances*. World Scientific.
17. Touzé C, Vizzaccaro A, Thomas O. 2021 Model order reduction methods for geometrically nonlinear structures: a review of nonlinear techniques. *Nonlinear Dynamics* **105**, 1141–1190.
18. Gilliatt HC, Strganac TW, Kurdila AJ. 2003 An investigation of internal resonance in aeroelastic systems. *Nonlinear Dynamics* **31**, 1–22.
19. Hong D, Hill TL, Neild SA. 2019 Conditions for the existence of isolated backbone curves. *Proceedings of the Royal Society A: Mathematical, Physical and Engineering Sciences* **475**, 20190374.
20. Givois A, Tan JJ, Touzé C, Thomas O. 2020 Backbone curves of coupled cubic oscillators in one-to-one internal resonance: bifurcation scenario, measurements and parameter identification. *Meccanica* **55**, 481–503.
21. Kerschen G, Peeters M, Golinval JC, Vakakis AF. 2009 Nonlinear normal modes, Part I: A useful framework for the structural dynamicist. *Mechanical systems and signal processing* **23**, 170–194.
22. Renson L, Kerschen G, Cochelin B. 2016 Numerical computation of nonlinear normal modes in mechanical engineering. *Journal of Sound and Vibration* **364**, 177–206.
23. Guillot L, Lazarus A, Thomas O, Vergez C, Cochelin B. 2020 A purely frequency based Floquet-Hill formulation for the efficient stability computation of periodic solutions of ordinary differential systems. *Journal of Computational Physics* **416**, 109477.

24. Rosenberg RM. 1960 Normal Modes of Nonlinear Dual-Mode Systems. *Journal of Applied Mechanics* **27**, 263–268.
25. Rosenberg RM. 1962 The Normal Modes of Nonlinear n-Degree-of-Freedom Systems. *Journal of Applied Mechanics* **29**, 7–14.
26. Shaw S, Pierre C. 1993 Normal Modes for Non-Linear Vibratory Systems. *Journal of Sound and Vibration* **164**, 85–124.
27. Haller G, Ponsioen S. 2016 Nonlinear normal modes and spectral submanifolds: existence, uniqueness and use in model reduction. *Nonlinear dynamics* **86**, 1493–1534.
28. Yabuno H, Kashimura T, Inoue T, Ishida Y. 2011 Nonlinear normal modes and primary resonance of horizontally supported Jeffcott rotor. *Nonlinear Dynamics* **66**, 377–387.
29. Hill TL, Cammarano A, Neild SA, Wagg DJ. 2015 Out-of-unison resonance in weakly nonlinear coupled oscillators. *Proceedings of the Royal Society A: Mathematical, Physical and Engineering Sciences* **471**, 20140659.
30. Lewandowski R. 1997 Computational formulation for periodic vibration of geometrically nonlinear structures—part 2: Numerical strategy and examples. *International Journal of Solids and Structures* **34**, 1949–1964.
31. Dankowicz H, Schilder F. 2013 *Recipes for continuation*. SIAM.
32. Peeters M, Viguié R, Sérandour G, Kerschen G, Golinval JC. 2009 Nonlinear normal modes, Part II: Toward a practical computation using numerical continuation techniques. *Mechanical systems and signal processing* **23**, 195–216.
33. Neild SA, Champneys AR, Wagg DJ, Hill TL, Cammarano A. 2015 The use of normal forms for analysing nonlinear mechanical vibrations. *Philosophical Transactions of the Royal Society A: Mathematical, Physical and Engineering Sciences* **373**, 20140404.
34. Golubitsky M, Stewart I, Schaeffer DG. 2012 *Singularities and Groups in Bifurcation Theory: Volume II* vol. 69. Springer Science & Business Media.
35. Wagg D, Neild S. 2016 *Nonlinear vibration with control*. Springer.
36. Kovacic I, Rand R, Mohamed Sah S. 2018 Mathieu's equation and its generalizations: overview of stability charts and their features. *Applied Mechanics Reviews* **70**.
37. Lazarus A, Thomas O. 2010 A harmonic-based method for computing the stability of periodic solutions of dynamical systems. *Comptes Rendus Mécanique* **338**, 510–517.
38. Ruby L. 1996 Applications of the Mathieu equation. *American Journal of Physics* **64**, 39–44.
39. Rand RH. 2005 *Lecture notes on nonlinear vibrations*. Dept. Theoretical and Applied Mechanics, Cornell University, Ithaca, NY.
40. Hill TL, Cammarano A, Neild SA, Barton DAW. 2017 Identifying the significance of nonlinear normal modes. *Proceedings of the Royal Society A: Mathematical, Physical and Engineering Sciences* **473**, 20160789.
41. Kuether RJ, Deaner BJ, Hollkamp JJ, Allen MS. 2015 Evaluation of Geometrically Nonlinear Reduced-Order Models with Nonlinear Normal Modes. *AIAA Journal* **53**, 3273–3285.
42. Nicolaidou E, Melanthuru VR, Hill TL, Neild SA. 2020 Accounting for quasi-static coupling in nonlinear dynamic reduced-order models. *Journal of Computational and Nonlinear Dynamics* **15**.
43. Shen Y, Béreux N, Frangi A, Touzé C. 2021 Reduced order models for geometrically nonlinear structures: Assessment of implicit condensation in comparison with invariant manifold approach. *European Journal of Mechanics - A/Solids* **86**, 104165.
44. Guckenheimer J, Holmes P. 2013 *Nonlinear oscillations, dynamical systems, and bifurcations of vector fields* vol. 42. Springer Science & Business Media.
45. Touzé C. 2014 Normal form theory and nonlinear normal modes: theoretical settings and applications. In *Modal analysis of nonlinear mechanical systems* pp. 75–160. Springer.
46. Nicolaidou E, Hill TL, Neild SA. 2021 Detecting internal resonances during model reduction. *Proceedings of the Royal Society A: Mathematical, Physical and Engineering Sciences* **477**, 20210215.
47. Kotowski G. 1943 Lösungen der inhomogenen Mathieuschen Differentialgleichung mit periodischer Störfunktion beliebiger Frequenz (mit besonderer Berücksichtigung der Resonanzlösungen). *ZAMM - Journal of Applied Mathematics and Mechanics / Zeitschrift für Angewandte Mathematik und Mechanik* **23**, 213–229.